Samia Afrin
Department of Engineering & Engineering Technology,
East Tennessee State University,
1276 Gilbreath Dr.,
Johnson City, TN 37614
e-mail: afrins@etsu.edu

Nazmul Hossain
Department of Mechanical Engineering,
University of Houston,
4800 Calhoun Road,
Houston, TX 77004
e-mail: nhossain3@uh.edu

Zhiwen Ma
Department of Mechanical Engineering,
National Renewable Energy Laboratory,
Golden, CO 80401
e-mail: zhiwen.ma@nrel.gov

V. M. Krushnarao Kotteda[1]
Mem. ASME
Department of Mechanical Engineering,
University of Wyoming,
1000 E. University Ave.,
Laramie, WY 82071
e-mail: vkotteda@uwyo.edu

Antara Badhan
Mem. ASME
Department of Environmental Science and Engineering,
University of Texas at El Paso,
500 W. University Ave.,
El Paso, TX 79968
e-mail: abadhan@miners.utep.edu

Vinod Kumar
Mem. ASME
Department of Mechanical Engineering,
University of Texas at El Paso,
500 W. University Ave.,
El Paso, TX 79968
e-mail: vkumar@utep.edu

On-Sun Testing of a High-Temperature Solar Receiver's Flux Distribution

Concentrated solar power (CSP) is a promising technology in transitioning to renewable energy because of its abundance in nature and thermal energy storage (TES) capability. Among the four types of available CSP technology, including parabolic trough, linear Fresnel, power tower, and parabolic dishes, a power tower using a central receiver has more potential to generate high-temperature heat in a scale supporting power cycles efficiency and achieve low levelized cost of energy (LCOE). Other than the conventional type of receiver design, the high-absorptive receiver concept developed and presented in this paper is novel in its design approach. The novel receiver design originated from National Renewable Energy Laboratory (NREL) consists of an array of solar flux absorb tubes. The solar absorb tubes require uniform flux distribution and in-depth flux penetration through the three different reflective sections of tubes in a hexagonal shape. To evaluate this unique receiver design and thermal performance, the flux distribution, flux uniformity, and intensity were numerically simulated using ANSYS FLUENT *and SolTrace modeling program. On-sun testing has been done at NREL high flux solar testing facility, based on the computational analysis.* [DOI: 10.1115/1.4052550]

Keywords: concentrating solar power, near blackbody receiver, solar flux intensity, flux distribution, clean energy, heat transfer, reflective coating materials, renewable, simulation

1 Introduction

Solar technology has a strong potential to meet our growing energy demand and reduce dependence on fossil fuels. The amount of energy being consumed by us is only of energy being intercepted by the earth [1]. Concentrated solar power (CSP) is a promising technology in the power generation sector because it provides grid-scale energy storage and enables greater renewable integration into the grid. One megawatt (MW) CSP plant can abstain 688 tons of CO_2 emission compared with the combined cycle system and 1360 tons of CO_2 emission if comparable with coal/steam cycle power plant [2].

Four types of CSP technologies are accessible these days, i.e., parabolic trough, linear Fresnel, sterling dish, and solar power tower. The solar power tower or central receiver CSP technology has more potential concerning high temperature, power block efficiency, and levelized cost of energy (LCOE) [3]. Here, sun rays hit the mirror surface called heliostats and reflected toward a high-temperature receiver where the concentrated rays transfer the heat energy to the heat transfer fluid (HTF). Concentrated solar flux impinging on the receiver allows the HTF to reach about 1000 °C temperature and then integrate this thermal energy into more efficient thermodynamic cycles for solar to electric power conversion.

Since 1970, the solar power tower concept has been developed. In 1982 near Barstow, California, Solar One, the 10 MW solar thermal central receiver pilot power plant, first started its operation [4]. After 6 years' successful testing and operation, it was decommissioned in 1988. The tubular liquid central receiver was operated by steam Rankine cycle with steam as the HTF, and the cycle efficiency was only 30% [5,6]. The HTF was switched to molten nitrate salt (60% sodium nitrate, 40% potassium nitrate) in the Solar Two power plant because of such a low efficiency and low heat transfer capacity of steam. This new HTF allowed higher incident flux [7] and better heat transfer, but molten nitrate salt cannot go beyond

[1]Corresponding author.

Contributed by the Solar Energy Division of ASME for publication in the JOURNAL OF SOLAR ENERGY ENGINEERING: INCLUDING WIND ENERGY AND BUILDING ENERGY CONSERVATION. Manuscript received April 22, 2021; final manuscript received September 18, 2021; published online October 19, 2021. Assoc. Editor: Peiwen Li.

565 °C, as it becomes unstable above that temperature. Liquid sodium [8], chloride salt [9], and fluoride salt [10] have also been proposed as an alternative HTF to molten nitrate salt. Carbonate salts have been suggested as an HTF because of their material compatibility and affordability, but at high temperatures, it degrades [11]. Another concern with liquid metals or salts is that they could freeze up (usually melting temperatures above ambient) due to equipment malfunction or operation error [12]. To alleviate this concern, the researcher projected to move on gaseous fluid at supercritical states like supercritical steam and supercritical carbon dioxide (sCO_2). Supercritical steam and sCO_2, while operated with a closed loop Brayton cycle, offers a power block efficiency of ~50% compared with the conventional subcritical steam Rankine cycle efficiency of 42% [13]. In addition, with addressing high-temperature issues, solid particles as an HTF can be used as thermal energy storage (TES) media to store energy to supply during peak hours. A particle-based CSP system was introduced to support the U.S. Department of Energy SunShot goal [14] and considered a Generation 3 CSP system [15]. Solid particles are favorable to other types of media like molten salt or gases. With its low cost, the same HTF can be used as storage media and high efficiency due to its' direct absorption feature [16]. A key component for a particle CSP system is the solid particle receiver (SPR) and its thermal performance.

Solid particles in a SPR behave in a granular flow pattern. The general concept is that particles are dropped from the top, irradiated by direct solar incident light from the heliostat field, get heated, and exit the receiver. Heated particles either exit through the heat exchanger or are directly stored as storage media in a tank. It has also been used for hydrogen production in Sandia National Laboratories; ceramic particle has dropped like a curtain from the top of the cavity receiver and heated up to 1000 °C. Sandia National Laboratories in Albuquerque made a prototype SPR. They have designed a cavity-type SPR where solid ceramic particles fall from the top of the tower following a certain shape and being exposed to the sun while passing through the receiver cavity. This group did on-sun testing at Sandia's National Solar Thermal Test Facility (NSTTF) field using carbo-bead particles and heated the particles over 900 °C by directly exposing them to concentrated sunlight [17].

Two types of tubular receivers are known in power tower technology: external and cavity-type receivers. Sandia designed their SPR with a cavity receiver concept, but National Renewable Energy Laboratory (NREL)'s design idea differs from the other conventional design. The design concept is very appropriate to its name, "Near-blackbody solid particle receiver." This receiver is designed as a stack of hexagonal shape tubes connected with its' flare section. Solid particles will flow across the back portion of the tube array and reach their desired high temperature. Therefore, solar flux distribution is the key factor in this design. This paper focuses on testing the solar flux distribution throughout the length of the hexagonal shape tube. For simplicity, only a single tube was numerically analyzed and tested in the NREL Solar Furnace Testing Facility for result validation. Though the irradiation was analyzed, the experimental work did not include the interaction of tubes in a tube array and the flow of particles. However, all relevant physical phenomena are considered in the numerical simulations.

2 Hexagonal Tube Geometry

The conceptual near-blackbody (NBB) receiver's novelty is that this design is divided into three different optical zones: front or flare section, middle section, and end section. Their optical properties and thermal stability distinguish these three sections at temperatures. The flare section is a highly specular surface but operable only at 150 °C, the middle section is a high hemispherical but a low specular reflective surface that can be thermally stable up to 1000 °C, and the end section is an oxidized metallic surface with 95% absorptivity at 1000 °C.

This receiver design considered a high specular reflective surface in its' front section at operating temperature 150 °C. This mirror finished specular surface helps penetrate the sunlight inside the hollow tube and increases the receiver's efficiency (Fig. 1). But at such an operating temperature and environmental condition, the optical properties degradation rate is high. The most commonly used mirror finished with high specular reflective material is silver (Ag) or Aluminum (Al) [18]. But the degradation rate under elevated conditions without a protection layer is rapid for both materials. Unprotected silver surfaces tend to degrade in ambient air, especially at elevated temperatures. Al is not a very good option to use because of its ability to scratch while handling.

3 Computational Modeling

Numerical analysis is subjected in this work to evaluate the design and performance testing of the near-blackbody solid particle receiver. Computational fluid dynamics (CFD) modeling software ANSYS 19.2 was used to study the performance of a single-tube hexagonal receiver among the hexagonal tube array for different configurations and inclination angles. The single-phase Eulerian approach with two other radiation models was found appropriate for solving the desired problem. A 3D single-tube hexagonal receiver was simulated with Surface-to-Surface (S2S) and Discrete Ordinates (DO) radiation models, coupled with solar ray tracing. Both models showed good agreement with experimental results. Temperature and heat flux distributions were observed for performance analysis and design consideration. NREL's SolTrace ray-tracing software was also used for mapping the heat flux on prototype receiver walls for on-sun testing conditions based on Sandia's NSTTF field and the solar furnace testing for a single-tube design.

3.1 Governing Equations for Fluid Flow and Radiation Modeling. The fluid flow pattern around the hexagonal tube is Eulerian-Eulerian or two-fluid model (TFM) computational problem. Eulerian-Eulerian approach is not suitable for tracking individual solid particles like the discrete element method (DEM). Here, both fluid and solid phases behave like interpenetrating with each other. This inter-phase exchange for each phase is solved by continuity and momentum equations.

$$\frac{\partial}{\partial t}(\alpha_i \rho_i) + \nabla.(\alpha_i \rho_i \overrightarrow{v_i}) = 0 \tag{1}$$

$$\frac{\partial}{\partial t}(\rho \vec{v}) + \nabla.(\rho \vec{v} \vec{v}) = -\nabla p + \nabla.(\bar{\bar{\tau}}) + \rho \vec{g} + \vec{F} \tag{2}$$

The energy equation to find the temperature field is

$$\frac{\partial}{\partial t}(\rho E) + \nabla.(\vec{v}(\rho E)) = \nabla.(k_{eff} \nabla T) + S_h \tag{3}$$

Surface-to-surface radiation model is considered when radiative heat transfer occurs between the granular particles and the surface of the tubes. FLUENT calculates the value of radiosity J and this value are then used to calculate the wall temperature of the faces in the cluster. The heat flux distribution is constant on each face, so the average temperature value of the surface cluster would not be impacted much by the highly nonlinear radiation source term (proportional to the fourth power of temperature). The following equation is used to calculate the average surface cluster temperature [19].

$$T_{SC} = \left(\frac{\sum_f A_f T_f^4}{\sum A_f} \right)^{\frac{1}{4}} \tag{4}$$

Here, T_{SC} is the surface cluster temperature, A_f is the area of face f, and T_f is the temperature of face f.

3.2 Soltrace Modeling. SolTrace is optical analyzing software developed at the NREL [20]. It has been used for performance analysis of solar power optical systems in CSP power plants. This ray-tracing tool models the heliostat field to map the heat flux

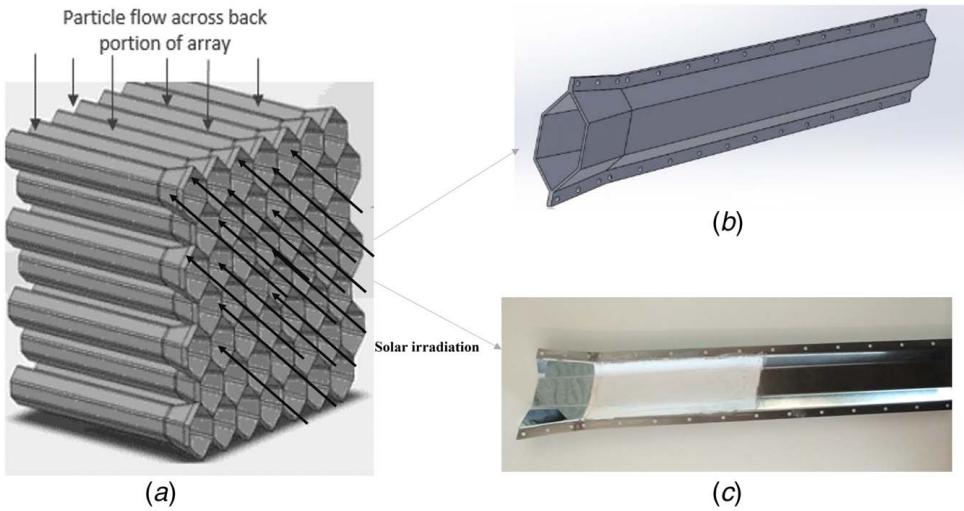

Fig. 1 (*a*) Schematic of a NBB receiver, (*b*) schematic of single hexagonal tube, and (c) cross section of a hexagonal tube. The backside is also a hexagonal cross section similar to the front side and a thin stainless-steel sheet.

distribution on high-temperature receivers. The accuracy of the result depends on the number of rays to be traced. The larger number of sun rays will give more accurate results but consume more processing time and be computationally expensive. It can resemble the heliostat field according to desired power output for a defined geographic location. It is a very handy software for scientific research in CSP applications.

Three right-handed coordinate systems have been used in SolTrace for optical characterization: the global coordinate system, the stage coordinate system, and the coordinate element system. Each element is defined according to its location and orientation in a stage coordinate system, i.e., local coordinate system. However, each stage coordinate system is defined as associating with its global coordinate system. Sun location is also specified based on the global coordinate system. The input of sun direction can be either in vector format or in time format with specified latitude. Figure 2 illustrates this phenomenon [21].

SolTrace modeling software aims to predict the solar flux map on the high-temperature receiver tubes, which may help guide the prototype design for fabrication and performance validation. It also envisions the reflective coating performance inside the tube wall through the flux mapping. A FORTRAN script compatible with SolTrace helps the flux map be readable for FLUENT SIMULATION software. Therefore, the flux map input in FLUENT can be comparable with the actual heliostat field instead of assuming constant heat flux throughout the tube. This boundary condition advantages to having more accurate results.

4 Soltrace Geometry

SolTrace modeling defined the sun shape for latitude 39.50, location Golden, Colorado; 180 days in the year. Heliostat position was calculated from global coordinates' origin and aim point location

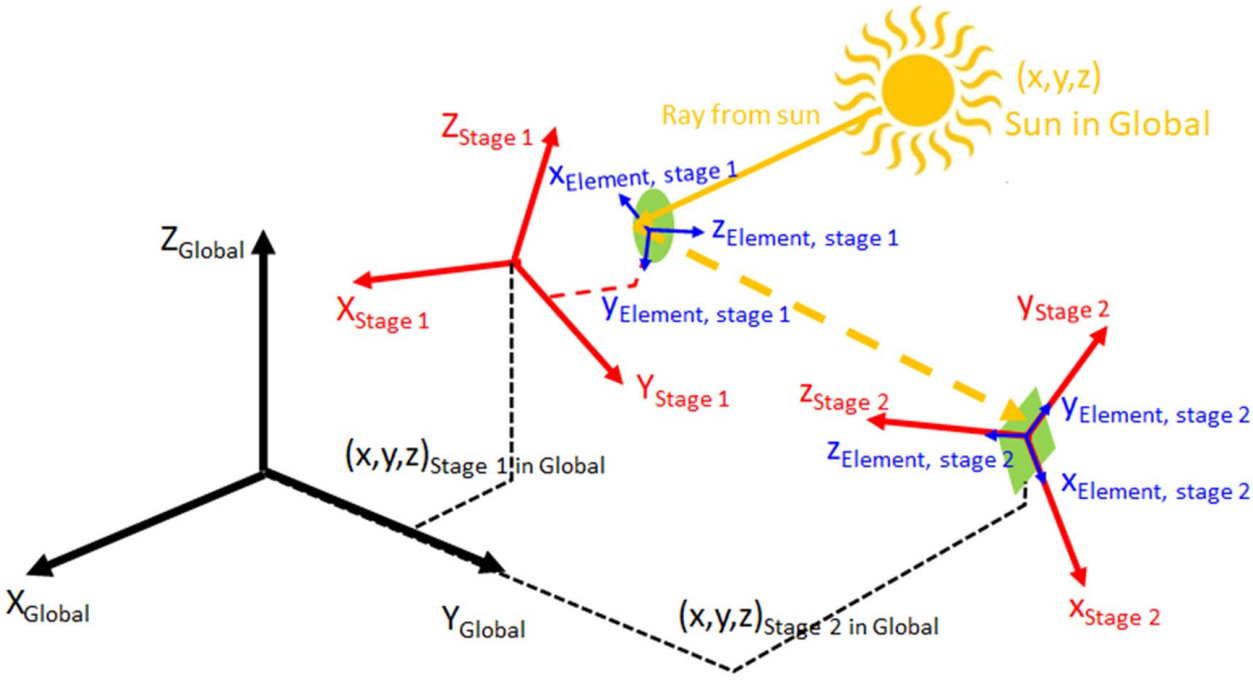

Fig. 2 Coordinate systems in SolTrace [21]

Table 1 Optical properties of three different coating zone

Sections	Length (in.)	Reflectivity	Transmissivity	Slope error (mrad)	Specularity error (mrad)
Flare	1.517	0.9250	1.0000	0.0001	200.00
Middle	5.18	0.8000	1.0000	2.0000	800.00
Back	6.303	0.1000	1.0000	2.0000	800.00

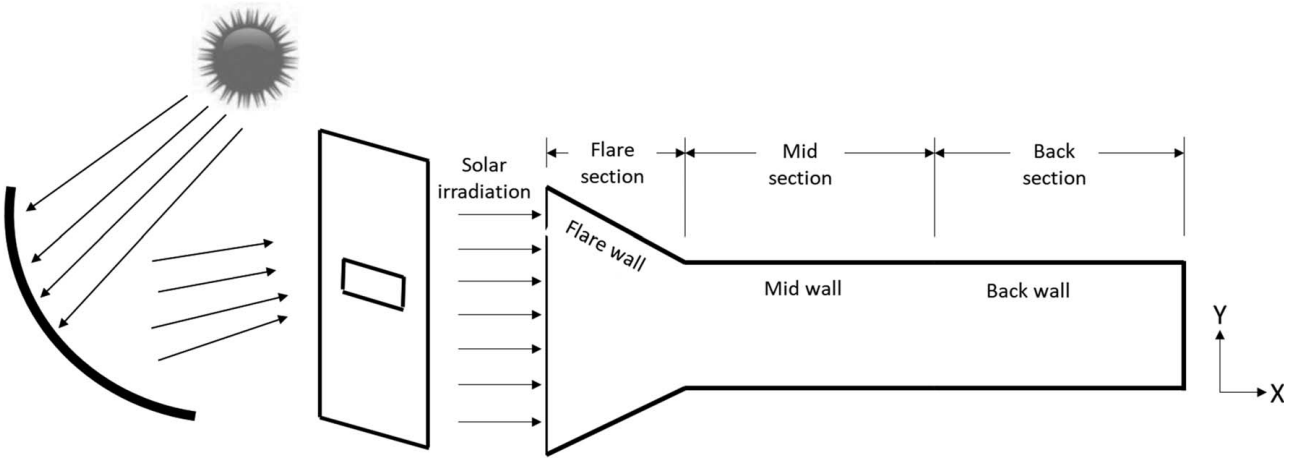

Fig. 3 Schematic diagram of the experimental setup

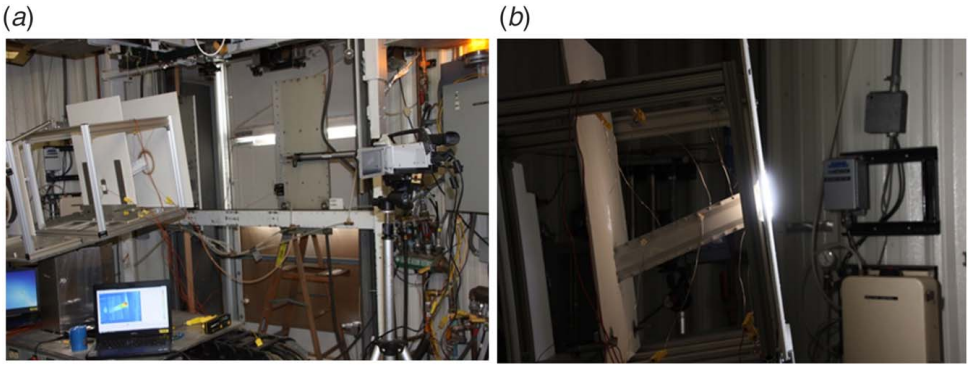

Fig. 4 (*a*) On-site testing at HFSF and (*b*) and ongoing testing with applied solar flux

for that specific day. Five system stages: heliostat, primary mirror array, attenuator, power plane, and hexagonal tube, were composed of several elements to replicate the solar furnace test setup. The hexagonal tube geometry was featured with a total number of 68 triangular elements. Tube length was divided into three sections distinguished by optical properties. The front of the flare section is a highly specular reflective surface, the middle section is a highly diffuse reflective surface, and the back part is an absorbent surface. Specularity error defines surface specular or diffuse characteristics for each section. Specular properties of the flare section aimed to help penetrate more flux and allow uniform flux to spread inside the tube. Table 1 contains the detail of optical properties. The number of rays to be traced is a function of result accuracy. For this case, the parameter was set at 2×10^6 number of ray intersections generated from the maximum of 2×10^8 sun rays [21]. Eight processors are used to speed up calculation. All calculation includes sun shape and optical errors.

5 High-Flux Solar Furnace Test Setup

The single-tube receiver is being tested at the NREL solar furnace testing facility, Golden, CO. It was hard to control a homogenous temperature distribution throughout the exposure time when concentrated solar radiation was directly applied to the sample. However, a shutter engaged in front of the concentrated beam operated from the control room to conduct the test. The function of this shutter was to temperature control and focus the concentrated beam to the tube axis. Figure 3 shows a schematic of the test setup. Figure 4(*a*) shows the on-sun testing setup at the High-Flux Solar Furnace (HFSF), and Fig. 4(*b*) shows the ongoing testing with applied solar flux. The frame was tilted to adjust the direction of the beam into the receiver. The concentrated beam of light comes into the test section at 7 deg angle. The tilting device can change the angle between the incident beam and tube axis from 0 deg to 20 deg angle. The focal point of the HFSF was located at the tube aperture. Two infrared (IR) cameras were put on each side of the tube to record the thermal images across the tube with the solar heating process. Type K thermocouples were located at the tube entrance, then 3 in. apart along the outside of the tube and one at the end cap, a thin stainless-steel sheet placed at the back end of the tube the solar flux on the tube end. The periphery outside the tube aperture was shielded with a high-temperature insulation board, such that the flux was only directed into the tube aperture, and the external sides of the tube were isolated from the solar flux. The focus of this work is the fabrication of one module and

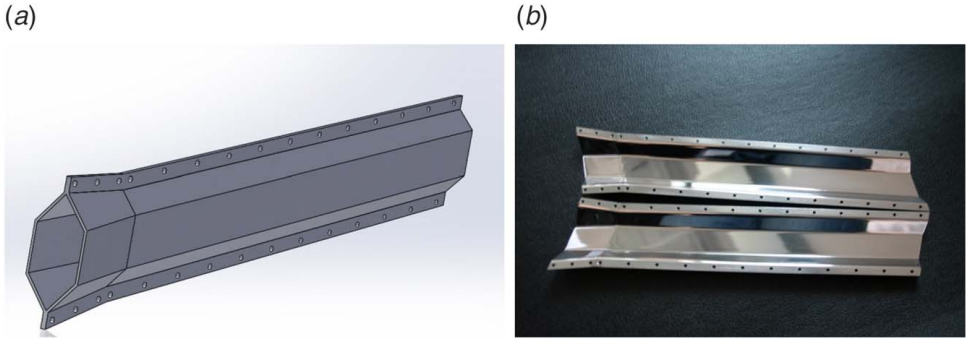

Fig. 5 (*a*) Schematic of an assembled single absorber tube and (*b*) mirror-polished SS single tube

Table 2 SolTrace output for each case

	SS tube w/o coating		SS polished tube		SS tube with Alanod	
Angle	Max flux (W/m^2)	Efficiency (%)	Max flux (W/m^2)	Efficiency (%)	Max flux (W/m^2)	Efficiency (%)
0	42,260.43	91.3689	28,914.32	98.7838	23,204.39	88.2803
5	37,790.39	91.5709	32,254.58	98.6277	39,263.07	89.0604
10	37,828.62	91.5368	42,265.94	98.4807	37,370.11	89.1492
15	33,404.46	91.2412	32,071.32	98.7005	32,258.04	88.2387
20	48,952.86	90.7236	44,488.25	98.8804	34,620.75	86.3561

the actual flux distribution measurements to model the system with particles in an adequate way.

5.1 Tube Fabrication. Three hexagonal shape absorber tubes were fabricated with different coating configurations. Every tube was manufactured into two parts so that the coating could be easily applied in the middle section of the tube. After fabrication, both parts were assembled by joining with the screws. Figure 5(*a*) is the schematic of an assembled single absorber tube, and Fig. 5(*b*) is a mirror-polished stainless-steel single absorber tube. The first tube was just the bare tube, the second one was mirror polished with 67% specular reflectivity, and the third one had three different coating zone. In the third tube, the front section or flare was glued with Alanod (specular reflectivity 95%). The middle section was sprayed with Al_2O_3 ceramic aerosol (hemispherical reflectivity 92%) tube end was oxidized at 800 °C. All three tubes were sprayed with white high-temperature silica-based ceramic coating for IR camera visualization.

5.2 Soltrace and Solar Furnace Test Result. The tested flux distribution was compared with modeled results. SolTrace modeling calculates the system's efficiency from the ratio of total hits of sun rays onto the system to the absorbed rays into the tube. The computer codes generated flux distribution data on the single-tube geometry and created Paraview Graphic Software files to visualize the flux spreading along the tube. Flux mapping facilitates the determination of the number of thermocouples and their locations for solar furnace testing. Each case is defined upon tube inclination angle, varied from 0 deg to 20 deg. SolTrace modeled flux distributions were plotted as Paraview contours in Table 2 to illustrate the flux spreading for the various incident angles. The contour plots depict that flux distribution spreads from the entrance at a small incident angle to more spreading at a 10-deg angle. SolTrace result shows a preliminary indication with the on-sun testing, and the model can be further verified with refined testing and modeling. The verified SolTrace model can then determine the input flux and tube inclination angle for prototype design and thus reduce on-sun testing risk and cost.

Table 2 explains the angular orientation effect on the efficiency of a single absorber tube. The first tube, which is a bare stainless-steel tube, showed 91.5709% efficiency for 5 deg position. The second tube with mirror-polished stainless-steel (specular reflectivity 67%) had a maximum of 98.8804% efficiency at 20 deg oblique position with the incident light. But, these two cases did not consider the end cap on tubes' end length; therefore the simulation result and the experimental result does not show a very good agreement. The third tube configuration, which has three different coating regions, shows best at 10 deg inclination angle. Then it starts to decrease in percentage, though not in a significant number. This simulation exactly mimics our test case 3 and matches the experimental result. The solar furnace testing set up different angles between the incident beam and the tube axis. The testing obtained the flux spreading for other coating conditions and the flux penetration relating to the angles between the incident beam and the tube axis.

The significance of this first-cut on-sun testing for an absorber tube at the NREL HFSF is validating the NBB receiver design basis—flux spreading along the tube wall under certain incident angles between the incoming solar flux, the tube axis, and the optical properties on the tube inner surfaces. Table 3 lists the measured tube maximum temperature, the ratio between the flux spreading depth and the tube aperture size, the thermal images from the infrared camera, and the flux distribution simulated from the SolTrace model under similar geometric settings.

The flux distribution images in Table 3 show that the 10 deg incident angle may be better than a smaller incident angle such as 0 deg or 5 deg. Though it looks very similar for 10 deg and 15 deg inclination, the 15 deg inclination angle has a higher flux density on one side than the other side of the tube. This result contradicts our original thought from the intuitive rationale that an aligned beam would penetrate deep in a tube. The discovery that a larger incident angle could get better flux spreading provides design flexibility in selecting the tube inclination angle. A smaller tilting angle can be adequate for the prototype design, and the small tube inclination can reduce the particle flow/heat transfer issues.

In Table 4, images in column 3 represent the IR camera image done by the solar furnace test, and column 4 is the flux distribution image from SolTrace simulation for polished stainless-steel tube

Table 3 Study of flux spreading on a three-zone fabricated tube for different angles and temperatures at the tube front

θ (deg)	T (°C)	Heat flux (IR camera)	Heat flux (SolTrace)
0	120	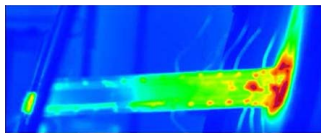	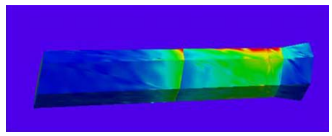
5	150	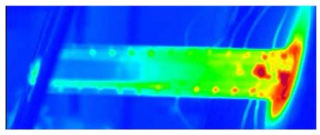	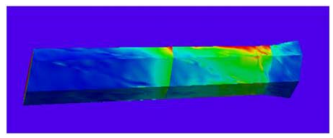
10	165	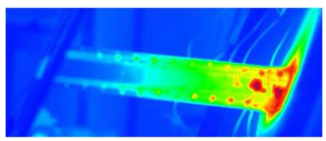	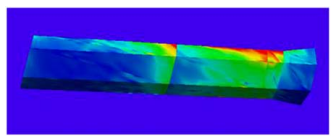
15	167	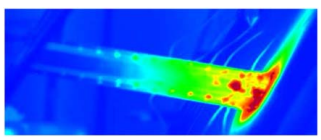	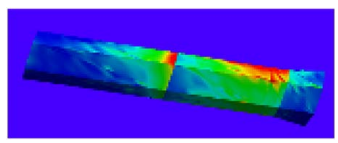
20	170	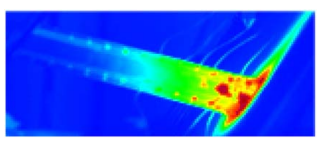	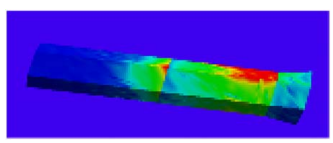

Table 4 Study of flux spreading on a polished stainless tube for different angles and temperatures at the tube front

θ (deg)	T (°C)	Temperature (IR camera)	Temperature (SolTrace)
0	120	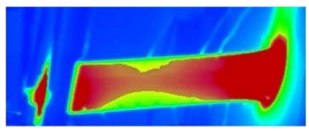	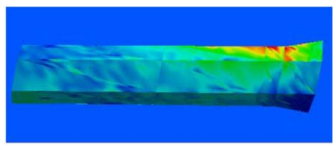
5	150	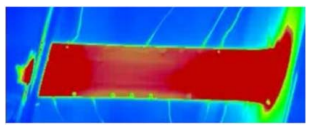	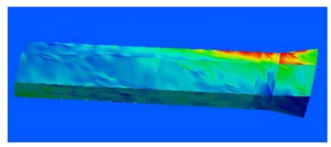
10	165	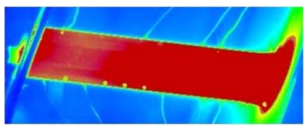	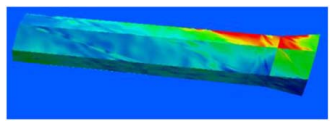
15	167	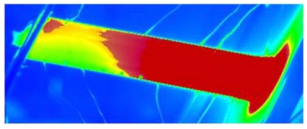	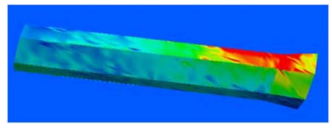
20	170	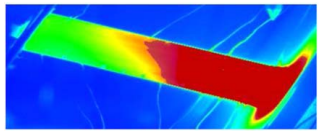	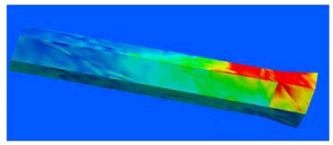

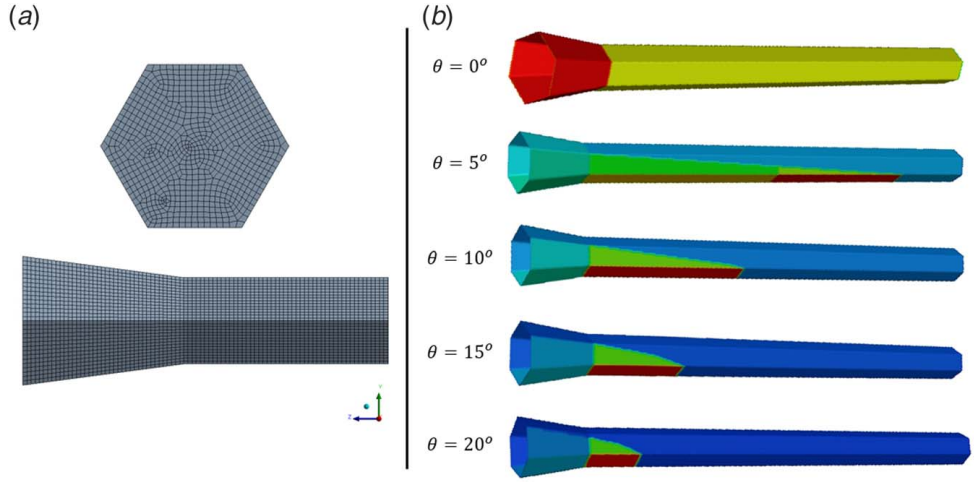

Fig. 6 (*a*) Computational mesh and (*b*) solar incident flux at different incident angles

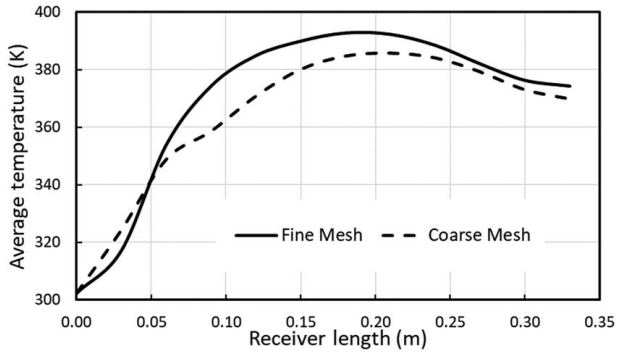

Fig. 7 Comparison of averaged cross-sectional temperature along the receiver length with two different computational meshes. The fine and coarse mesh contains approximately 8500k and 550k elements, respectively. In DO model, the direct solar irradiation is 5800 W/m^2 and θ = 0 deg

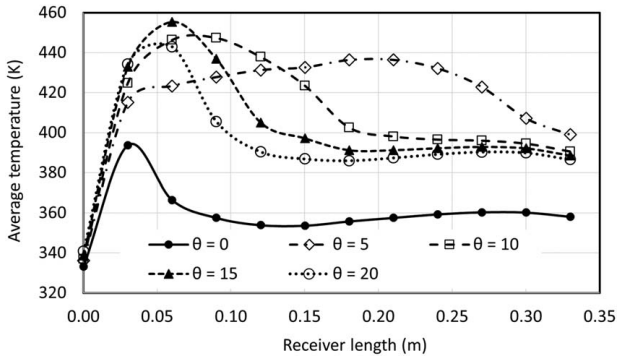

Fig. 9 SS polished tube (case-2): the variation of average temperature along receiver length for incident angles in the range of 0–20 deg. The direct solar irradiation is 5800 W/m^2 and the wall absorptivity is 0.67.

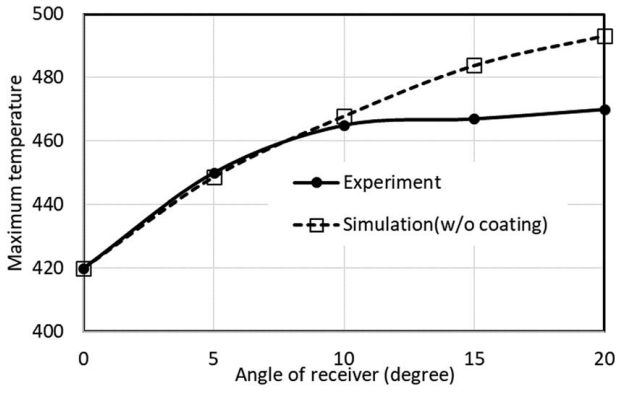

Fig. 8 SS polished tube (case-2): comparison of maximum temperature from experiments and numerical simulations for receiver angle in the range of 0–20 deg. The direct solar irradiation is 5800 W/m^2 and the opaque wall absorptivity is 0.67.

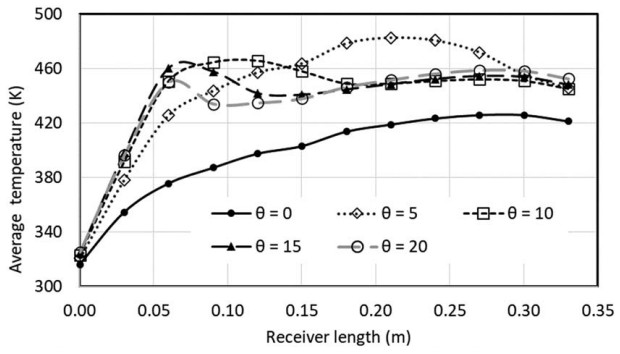

Fig. 10 SS tube with Alanod (case-3): the variation of average temperature along receiver length for incident angles in the range of 0–20 deg. The direct solar irradiation is 5800 W/m^2 and the wall absorptivity at flare, mid, and back sections are 0.075, 0.65, and 0.95, respectively.

fabrication. For tube tilting angle <15 deg, a single hexagonal tube with polished stainless-steel configuration shows an identical result (Table 4). Unlike 5 deg and 10 deg tube inclination angles, flux does not have uniform distribution through the tube when it is co-axial.

6 Numerical Analysis

Numerical analysis with ANSYS FLUENT 19.2 was done on a single-tube hexagonal receiver. A 3D model of the receiver was found to be more appropriate for this problem. Both Surface to Surface (S2S) and DO radiation model, coupled with Solar Ray Tracing to imitate

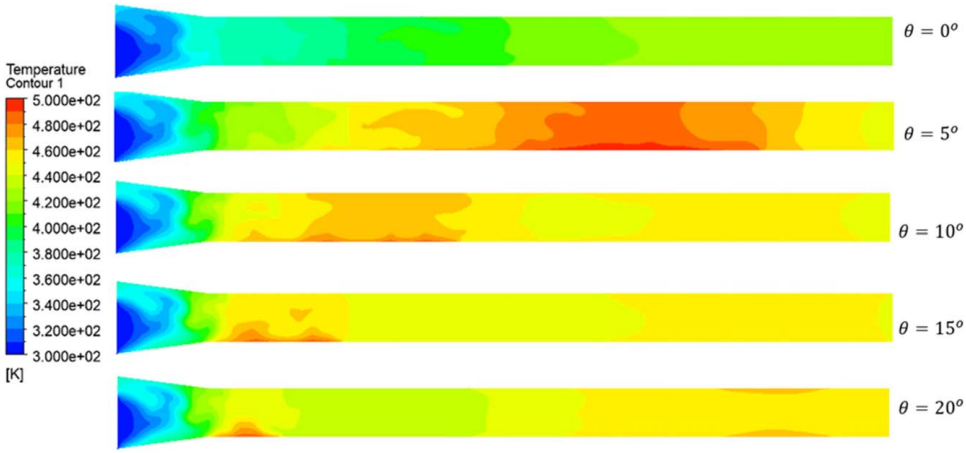

Fig. 11 SS tube with Alanod (case-3): cross-sectional temperature fields of receiver for incident angles in the range of 0–20 deg. The direct solar irradiation is 5800 W/m^2 and the wall absorptivity at flare, mid, and back sections are 0.075, 0.65, and 0.95, respectively.

the incoming solar flux was used to analyze. Both models showed similar results. The receiver walls are considered opaque with different specular reflectivity and absorptivity. The temperature fields for different incident angles of solar irradiation are studied. For the simulations, Solar irradiation of 5800 W/m^2 was used as an incoming solar flux. A solar vector was used to study solar flux at five different angles instead of a solar calculator. Figure 6 shows the front and side views of the coarse mesh. Figure 7 shows a comparison of averaged cross-sectional temperature with two different computational meshes.

The model was validated using the maximum temperature of the receiver from experimental data. Figure 8 shows the comparison. As we can see, the model shows excellent agreement with the experimental values. The slight deviation of maximum temperature at 15 deg and 20 deg are thought to be due to the positioning of sensors during the experiment. Three types of receivers have been considered for the experiment. They are classified based on the coating on receiver surface, which is related to specular reflectivity and absorptivity of the receiver walls. Here, we considered the following three cases for analysis:

- Case-1 is SS tube without coating.
- Case-2 is SS polished tube.
- Case-3 is SS tube with Alanod (three types of coating).

Figures 9 and 10 show average cross-sectional temperature along receiver length at different angles for case-2 and case-3. Both Figs. 9 and 10 show that the performance at 5 deg, to be the best due to maintaining the highest temperature along the mid and back section. And higher temperature distribution for case-3 than case-2 is observed. Figure 11 shows the cross-sectional temperature distribution of the receiver at different angles. This also gives us a similar conclusion that performance should be optimum at 5 deg incident angle for this size of receiver. This analysis can be implemented to design a better hexagonal receiver and optimize performance.

7 Conclusion

The design and performance of the receiver with arrays of hexagonal solar absorption tubes have been analyzed by using the SolTrace numerical simulation model. The modeling study varied angles between the absorber tube axis and the incoming beamline. The result indicates that the designed receiver would perform best at 5 deg between the absorber axis and the solar flux incident angle. Also, case studies of different coating arrangements have been investigated. From the analysis, we should have the best performance for case-3. The testing results verify the flux spreading mechanism in the NBB receiver design and provide confidence in selecting the proper receiver-tube inclination angle. However, the first-cut test in a tight schedule due to preparation and weather conditions reported the preliminary correlation between the thermal image and the modeled flux.

Acknowledgment

This work was sponsored by National Renewable Energy Laboratory under the award ZGG-5-52122-01 which is granted by the U.S. Department of Energy award no. DE-EE0001586. We would also like to acknowledge Judy Netter, Researcher III-Mechanical Engineering, NREL, who supported to setup the experimental work.

Conflict of Interest

There are no conflicts of interest.

Nomenclature

p = static pressure
E = internal energy
J = radiosity
S = source term
$\vec{v}$ = velocity vector
$\vec{F}$ = external body forces
A_f = area of face f
T_f = temperature of face f
T_{SC} = surface cluster temperature
keff = thermal conductivity
Ag = Silver
Al = Aluminum

Greek Symbols

αi = void fraction of phase i
θ = incident angle
$\rho\vec{g}$ = gravitational body force
$\bar{\tau}$ = stress tensor

References

[1] Edenhofer, O., Pichs-Madruga, R., Sokona, Y., Seyboth, K., Matschoss, P., Kadner, S., and Zwickel, P., IPCC, 2011, Cambridge University Press, Cambridge, UK and New York.
[2] European Academies Science Advisory Council, 2011, EASAC Policy Report 16.
[3] Muller-Steinhagen, H., and Trieb, F., 2004, "Concentrating Solar Power, a Review of the Technology," Ingenia, **18**(18), pp. 43–50.

[4] Radosevich, L. G.,1988, Final Report on the Power Production Phase of the 10 MWe Solar Thermal Central Receiver Pilot Plant, Sandia National Laboratories, Albuquerque, NM, Report SANDS87-8022.
[5] Alpert, D.J., and Kolb, G.J.,1988, Performance of the Solar One Power Plant as Simulated by the SOLERGY Computer Code, Sandia National Laboratories, Albuquerque, NM, Report SAND88-0321.
[6] Fleming, A., Folsom, C., Ban, H., and Ma, Z., 2017, "A General Method to Analyze the Thermal Performance of Multi-Cavity Concentrating Solar Power Receivers," Sol. Energy, **150**(1), pp. 608–618.
[7] Hale, M. J.,1999, Solar Two Performance Evaluation, National Renewable Energy Lab., Golden, CO (US), Vol. 1, No. NREL/CP-550-26642.
[8] Falcone, P., 1986, *A Handbook for Solar Central Receiver Design*, Sandia National Lab., Livermore, CA.
[9] Singer, C., Buck, R., Pitz-Paal, R., and Müller-Steinhagen, H., 2010, "Assessment of Solar Power Tower Driven Ultrasupercritical Steam Cycles Applying Tubular Central Receivers With Varied Heat Transfer Media," ASME J. Sol. Energy Eng., **132**(4), p. 041010.
[10] Forsberg, C. W., Peterson, P. F., and Zhao, H., 2007, "High-Temperature Liquid-Fluoride-Salt Closed-Brayton-Cycle Solar Power Towers," ASME J. Sol. Energy Eng., **129**(2), pp. 141–146.
[11] Stern, K. H., 2001, *High Temperature Properties and Thermal Decomposition of Inorganic Salts With Oxyanions*, 1st ed., CRC Press, Boca Raton, FL.
[12] Mancini, T. R., Gary, J. A., Kolb, G. J., and Ho, C. K.,2011, Power Tower Technology Roadmap and Cost Reduction Plan, Sandia National Laboratories, Albuquerque, NM, Report No. SAND2011–2419.
[13] Ho, C., and Iverson, B.,2012, Review of Central Receiver Designs for High-Temperature Power Cycles, Sandia National Laboratories, Albuquerque, NM, SAND2012-8379C.
[14] Ma, Z., Glatzmaier, G., and Mehos, M., 2014, "Fluidized Bed Technology for Concentrating Solar Power With Thermal Energy Storage," ASME J. Sol. Energy Eng., **136**(3), p. 031014.
[15] Mehos, M., Turchi, C., Vidal, J., Wagner, M., Ma, Z., Ho, C., Kolb, W., Andraka, C., and Kruizenga, A.,2017, Concentrating Solar Power Gen3 Demonstration Roadmap, National Renewable Energy Laboratory (NREL), Golden, CO, Technical Report NREL/TP-5500-67464.
[16] Siegel, N., Kolb, G., Kim, K., Rangaswamy, V., and Moujaes, S., 2007, "Solid Particle Receiver Flow Characerization Studies," ASME 2007 Energy Sustainability Conference, Long Beach, CA, July 27–30, pp. 877–883.
[17] Siegel, N. P., Ho, C. K., Khalsa, S. S., and Kolb, G. J., 2010, "Development and Evaluation of a Prototype Solid Particle Receiver: On-Sun Testing and Model Validation," ASME J. Sol. Energy Eng., **132**(2), p. 021008.
[18] Morris, V. L., 1980, "Cleaning Agents and Techniques for Concentrating Solar Collectors," Sol. Energy Mater., **3**(1–2), pp. 35–55.
[19] ANSYS Inc, 2013, *Ansys Fluent 15.0 User's Guide*, ANSYS, Inc., Canonsburg, PA.
[20] Wendelin, T., 2003, "SolTRACE: A New Optical Modeling Tool for Concentrating Solar Optics," ASME 2003 International Solar Energy Conference, Kohala Coast, HI, Mar. 15–18, pp. 253–260.
[21] Wendelin, T., Dobos, A., and Lewandowski, A.,2013, SolTrace: A Ray-Tracing Code for Complex Solar Optical Systems, National Renewable Energy Laboratory (NREL), Golden, CO, Technical Report NREL/TP-5500-59163.